Magnetic-Field-Assisted Spectral Decomposition and Imaging of Charge States of N-V Centers in Diamond

T. Chakraborty,[1,*,§] R. Bhattacharya,[2] V.S. Anjusha,[2,3] M. Nesladek,[4,5] D. Suter,[1,2,†] and T.S. Mahesh[2,‡]

[1] *Fakultät Physik, Technische Universität Dortmund, Dortmund 44221, Germany*
[2] *Department of Physics and NMR Research Center, Indian Institute of Science Education and Research, Pune 411008, India*
[3] *Institut for Quantum Optics, Ulm University, Albert-Einstein-Allee 11, Ulm 89081, Germany*
[4] *Institute for Materials Research (IMO), Hasselt University, Diepenbeek, 3590 Belgium*
[5] *IMOMEC Division, IMEC, Diepenbeek 3590, Belgium*

(Received 24 March 2021; revised 19 June 2021; accepted 16 December 2021; published 16 February 2022)

With the advent of quantum technology, nitrogen vacancy (N-V) centers in diamond turn out to be a frontier that provides an efficient platform for quantum computation, communication, and sensing applications. Due to the coupled spin-charge dynamics of the N-V system, knowledge of N-V charge-state dynamics can help to formulate efficient spin-control sequences strategically. Here, we report two spectroscopy-based deconvolution methods to create charge-state mapping images of ensembles of N-V centers in diamond. First, relying on the fact that an off-axis external magnetic field mixes the electronic spins and selectively modifies the photoluminescence (PL) of N-V^-, we perform decomposition of the optical spectrum for an ensemble of N-V and extract the spectra for N-V^- and N-V^0 states. Next, we introduce an optical-filter-based decomposition protocol and perform PL imaging for N-V^- and N-V^0. Previously obtained spectra for N-V^- and N-V^0 states are used to calculate their transmissivities through a long-pass optical filter. These results help us to determine the spatial distribution of the N-V charge states in a diamond sample.

DOI: 10.1103/PhysRevApplied.17.024046

I. INTRODUCTION

By virtue of having remarkable quantum properties at room temperature and a spin-dependent optical response, the nitrogen-vacancy (N-V) center in diamond provides an efficient platform to implement protocols of quantum technology [1,2]. A long coherence time [3], photostable single-photon-emitting capability [4], the possibility of addressing and manipulating spins via optical and microwave excitation [5–7], the possibility to read out the spin states by different methods [8], and efficient integrability into photonic structures [9] have led to applications of N-V centers in several aspects of quantum technology. Notably, N-V centers exhibit promising applications in quantum-information processing [10,11], magnetometry [12,13], biosensing [14,15], thermometry [16,17], and so on. The negatively charged state of the N-V center (N-V^-) is widely investigated, allowing optical- and microwave-excitation-controlled preparation, manipulations, and readout of its spin states in an efficient way, whereas qubits associated with the neutral charge state (N-V^0) and their quantum control have not been well-explored experimentally, although theoretical proposals have been put forward [18,19].

In magnetometry applications, ensembles of N-V^- centers being operated under ambient conditions show excellent efficiency in field imaging with high spatial resolution [14,20] and sensitivity up to 1 pT/$\sqrt{\text{Hz}}$ [13,21]. An ensemble of N N-V centers can generate N times the number of photons per unit time compared with a single center, and therefore, increases the sensitivity by a factor of $\sqrt{N}$ [12]. Moreover, an ensemble of N-V with four different crystal orientations allows one to perform direction-sensitive magnetic field sensing [22]. Although N-V^- is the target state for sensing applications, the sensitivity is reduced by the presence of the neutral charge state, as N-V^0 centers add a spin-independent photoluminescence (PL) background to the desired signal, which affects the field-detection sensitivity [23]. The N-V photophysics results in an interconversion dynamics between these two

*t.chakraborty-1@tudelft.nl
†Dieter.Suter@tu-dortmund.de
‡mahesh.ts@iiserpune.ac.in
§Current address: QuTech and Kavli Institute of Nanoscience, Delft University of Technology, Delft 2600 GA, Netherlands.

charge states [24]. Thus, the N-V^- spin properties, and hence, the sensing efficiency, is affected by the coupled spin-charge dynamics of the N-V^0–N-V^- composite system [25–28].

The concentration of N-V^- and N-V^0 centers can vary in different diamond samples, depending on the preparation conditions and processing parameters [29]. In fact, for a given diamond substrate, there can be a local variation of the charge-state ratio, depending on local crystal strain, impurities, the crush force, and so on [30]. Moreover, as a function of various parameters, like optical power, magnetic field, illumination wavelength [24,25], and temperature [31], interconversion mechanisms of ionization and recombination [24] are involved, which cause N-V^- $\rightarrow$ N-V^0 and N-V^0 $\rightarrow$ N-V^- conversions, respectively. Since the charge-state conversion (CSC) influences the N-V spin-relaxation behavior, and hence, its sensing efficiency, it is required to tailor the CSC dynamics by tuning the above-mentioned parameters in such a way that the sensitivity is maximized. In this context, it is necessary to obtain a quantitative picture of N-V^- and N-V^0 charge states of the N-V ensemble under given experimental conditions.

Here, we demonstrate easily implementable yet powerful methods to decompose the spectra of N-V centers into the contributions from the N-V^- and N-V^0 oxidation states. Earlier reports have demonstrated spectral decomposition for N-V charge states by modifying the N-V^- PL signal using a microwave field that is resonant between the $m_S = 0$ and -1 states [23] and by studying a number of diamond samples with varying concentrations of charge states [32]. However, in this work, we use the fact that an external magnetic field influences the optical pumping process of N-V centers to perform spectral decomposition. We demonstrate PL mapping of N-V^0 and N-V^- using the field-assisted method and an optical-filter-based approach. The transmitivities of the N-V^0 and N-V^- spectra through the optical filter are required as inputs in the second method. Here, we use the decomposed spectra to calculate the transmitivities of N-V^0 and N-V^- signals. However, to apply the filter-based charge-state imaging method, one does not necessarily have to generate the N-V^0 and N-V^- spectra; rather, the spectra can be obtained from the literature and the transmitivities can be calculated. Both protocols have the flexibility that they can be applied for different diamond samples and under various experimental conditions, like temperature, magnetic field, optical power, or illumination wavelength.

Based on the fact that an off-axis external magnetic field reduces the N-V^- spin polarization, and hence, the PL intensity of the optical spectra, we perform spectral decomposition to separate out N-V^0 and N-V^- charge states in the spectrum. Next, we determine the transmissivity of the PL signal from N-V^0 and N-V^- through an optical filter and use it in our spectral decomposition protocol to create charge-state mapping images for N-V^0 and N-V^- centers.

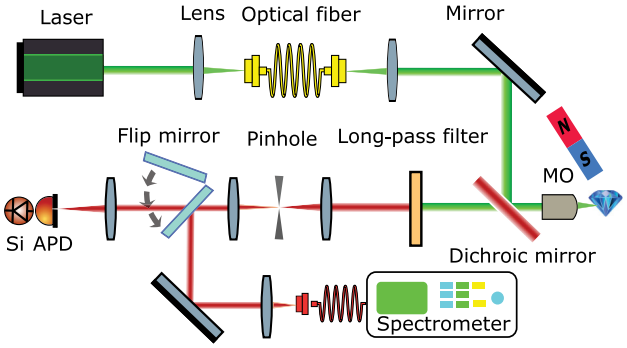

FIG. 1. Schematic diagram of the home-built confocal setup, which is combined with a spectrometer. Permanent magnet is used to apply the magnetic field to the N-V system.

II. EXPERIMENTAL METHOD

Our experiments are performed in a home-built experimental setup, where confocal microscopy is combined with optical spectroscopy. We measure ensembles of N-V embedded in a diamond layer, which is grown by chemical vapor deposition on a ⟨100⟩-oriented type-Ib single-crystal diamond substrate, electron irradiated (energy $\sim$ 16.5 MeV, fluence $\sim 8 \times 10^{17}$ cm^{-2}), and annealed (at 700 °C for 45 min and at 1000 °C for 90 min). The N-V concentration for this sample is 20 ppm, which is estimated by measuring the PL counts and by comparing them with the counts obtained for a sample with known N-V concentration under the same experimental conditions. Figure 1 shows a simplified schematic diagram of our experimental setup. We use a diode-pumped 532-nm solid-state laser to excite the N-V centers. A high-numerical-aperture (NA = 1.3) microscope objective (MO) tightly focuses the excitation beam onto the diamond sample. To create PL mapping images of the sample, the MO is mounted on a nanopositioning piezo stage, which has a traveling range of 100 $\times$ 100 μm^2 in the X-Y plane and 20 μm along the Z axis. The PL signal from the sample is collected by the same MO; separated from the reflected laser signal by a dichroic mirror and a long-pass 550-nm filter; and passes through a pinhole, which rejects any out-of-focus signal. Next, the signal is collimated using a lens and detected by a Si avalanche photodiode (APD), which is sensitive at the single-photon level. For optical spectroscopy measurements, we use a flip mirror to couple the signal to the input slit of a CCD spectrometer through an optical fiber.

III. DECOMPOSITION OF OPTICAL SPECTRA INTO N-V^0 AND N-V^-

The PL emission from an N-V center varies with the strength and orientation of an external magnetic field [33–35]. The dependence differs for two relevant charge states, as discussed below. In the absence of a magnetic field, the N-V^- system is initialized to the $m_S = 0$

state by optical illumination. However, application of a magnetic field that is not parallel to the N-V symmetry axis influences the optical pumping process, which results in a redistribution of population in the electronic spin levels $m_S = 0$ and ± 1; this is termed spin mixing [33,34]. An increase in the strength of the applied field enhances spin mixing. Hence, the probability of nonradiative transitions from the excited $m_S = \pm 1$ states to the ground state through the metastable singlet state increases, which leads to a decrease in the N-V^- PL signal [33,34]. Application of a 600-G field along the [100] axis of a diamond crystal completely depolarizes the electronic spins, which can be referred to as a fully-spin-mixed state. Although a change in the applied magnetic field strength influences the ionization process, the relative populations of the N-V^0 and N-V^- charge states do not change [26]. As a result, the change in strength of the magnetic field does not affect the N-V^0 PL intensity for an N-V ensemble [26].

We use this charge-state-selective change in the PL signal due to an off-axis magnetic field to separate the contributions from N-V^0 and N-V^- to the measured PL spectra for an N-V ensemble. Under constant excitation with a 532-nm laser, we measure spectra of an N-V ensemble at different strengths of magnetic field that is not parallel to the N-V axis. We measure N-V centers, the axes of which are equally distributed along the four possible crystallographic directions in a diamond crystal oriented in the [100] direction. The magnetic field is applied along the [100] direction of the diamond crystal, making equal angles with the four different N-V orientations. To reduce the effect of optical and electrical noise, each measurement is averaged over 3000 nominally identical spectra. For each scan, the measurement time is 10 ms and the laser intensity is 4.8 mW μm^{-2}. To make sure that the applied field results in notable spin mixing, and we can capture an observable change in N-V^- PL as a function of the field, we vary the magnetic field through a large range ($\approx$ 800 G) of steps, keeping its direction fixed, and measuring the spectra. As long as the spectra captured at the field values give a significant change in N-V^- PL, and therefore, a high signal-to-noise ratio (SNR), the analysis can be performed. The low field does not necessarily have to be the zero field. We denote the spectra measured at low and high fields as $A_{\text{low}\,\mathbf{B}}(\lambda)$ and $A_{\text{high}\,\mathbf{B}}(\lambda)$, respectively; they are shown in Fig. 2(a).

We write the spectrum at low field ($\approx$ 170 G) as a composition of the N-V^- and N-V^0 spectra $A_{\text{N-}V^0}(\lambda)$ and $A_{\text{N-}V^-}(\lambda)$, respectively:

$$A_{\text{low}\,\mathbf{B}}(\lambda) = A_{\text{N-}V^0}(\lambda) + A^{\text{low}\,\mathbf{B}}_{\text{N-}V^-}(\lambda). \tag{1}$$

We aim to decompose $A_{\text{low}\,\mathbf{B}}(\lambda)$ into $A_{\text{N-}V^0}(\lambda)$ and $A^{\text{low}\,\mathbf{B}}_{\text{N-}V^-}(\lambda)$. In $A_{\text{high}\,\mathbf{B}}(\lambda)$, the N-$V^-$ PL intensity is selectively modified by enhancing spin mixing with a higher magnetic field ($\approx$ 975 G), while the N-V^0 signal is not significantly

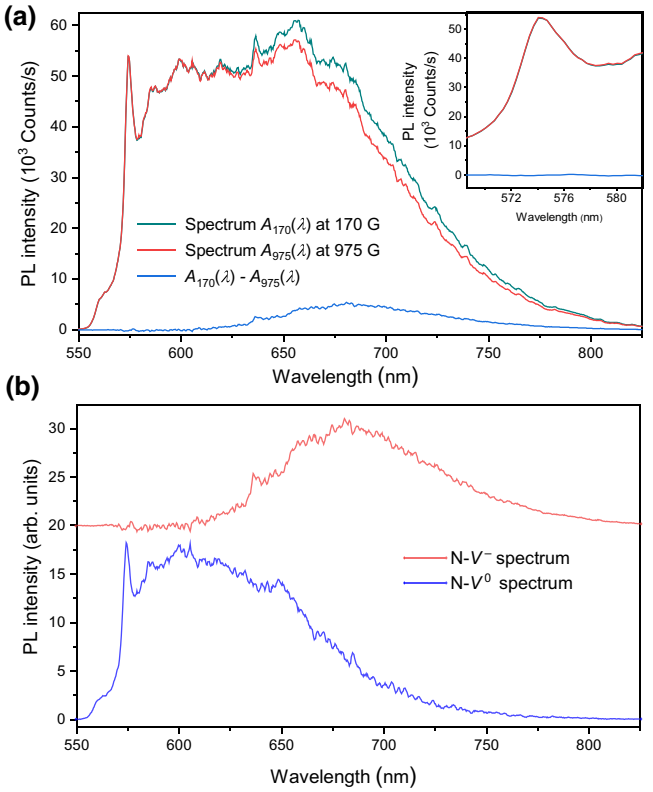

FIG. 2. (a) Measured N-V emission spectra at low ($\sim$ 170 G) and high ($\sim$ 975 G) magnetic fields shown by green and red curves, respectively. Spectra show the ZPL for N-V^0 at 575 nm and for N-V^- at 637 nm. Blue curve denotes the spectrum obtained by subtracting the spectrum at high field from the one recorded at low field. Inset shows an expanded view of the region near the N-V^0 ZPL. (b) Extracted N-V^0 (blue curve) and N-V^- spectra (red curve). N-V^- spectrum is manually shifted along the y axis to make both spectra visible.

affected, as discussed earlier. Hence, one can express

$$A_{\text{high}\,\mathbf{B}}(\lambda) = A_{\text{N-}V^0}(\lambda) + A^{\text{high}\,\mathbf{B}}_{\text{N-}V^-}(\lambda), \tag{2}$$

where $A^{\text{high}\,\mathbf{B}}_{\text{N-}V^-}(\lambda)$ is the PL contribution to the total spectrum from N-V^- centers at high field. We quantify the change in the N-V^- signal as $\Delta_{\text{N-}V^-}$, as a result of changing the field by subtracting $A_{\text{high}\,\mathbf{B}}(\lambda)$ from $A_{\text{low}\,\mathbf{B}}(\lambda)$:

$$\begin{aligned}\Delta_{\text{N-}V^-} &= A_{\text{low}\,\mathbf{B}}(\lambda) - A_{\text{high}\,\mathbf{B}}(\lambda),\\ &= A^{\text{low}\,\mathbf{B}}_{\text{N-}V^-}(\lambda) - A^{\text{high}\,\mathbf{B}}_{\text{N-}V^-}(\lambda).\end{aligned} \tag{3}$$

Figure 2(a) reveals that $\Delta_{\text{N-}V^-}$ does not show any signature of N-V^0 zero-phonon line (ZPL). The inset of Fig. 2(a) shows an enlarged view of the ZPL for $A_{\text{low}\,\mathbf{B}}(\lambda)$, $A_{\text{high}\,\mathbf{B}}(\lambda)$, and $\Delta_{\text{N-}V^-}$, and in the presence of low and high magnetic fields, where one can observe hardly any difference in ZPL intensity between these two cases. Since the $\Delta_{\text{N-}V^-}$ data contain the PL contribution solely from N-V^-

centers, it is possible to determine a scaling factor, f, a real positive number, such that the following two equations are satisfied:

$$A^{\text{low}\,\mathbf{B}}_{\text{N-}V^-}(\lambda) = f\,\Delta_{\text{N-}V^-}, \tag{4}$$

$$A_{\text{N-}V^0}(\lambda) = A_{\text{low}\,\mathbf{B}}(\lambda) - f\,\Delta_{\text{N-}V^-}. \tag{5}$$

Proper evaluation of factor f determines the efficiency of the decomposition analysis by assuring that $A_{\text{N-}V^0}(\lambda)$ and $A^{\text{low}\,\mathbf{B}}_{\text{N-}V^-}(\lambda)$ do not have any contributions from the PL of N-V^- and N-V^0, respectively. For this purpose, we follow a trial-and-error optimization method, where we vary the value of f in small steps, and for each value of f, the operations described in Eqs. (4) and (5) are performed. We find $f = 6.2$ to be optimal. A higher or lower value results in a dip or peak at 637 nm, the ZPL of N-V^-, in the $A_{\text{N-}V^0}(\lambda)$ curve. Using $f = 6.2$ in Eqs. (4) and (5), we can obtain the individual spectra of $A^{\text{low}\,\mathbf{B}}_{\text{N-}V^-}(\lambda)$ and $A_{\text{N-}V^0}(\lambda)$, which are shown in Fig. 2(b).

We perform the decomposition of N-V spectra into N-V^0 and N-V^- for a range of magnetic field values and use these results to study the field dependence of the PL from N-V^0 and N-V^-. This analysis also provides us a quantitative estimation of the scaling factor, f, for a change in magnetic field from B_1 to B_2, where $B_2 > B_1$. We express the N-V spectra, $A_{\text{N-}V}(\lambda)$, as a linear combination of the contributions from N-V^0 and N-V^- emissions in the following way:

$$A_{\text{N-}V}(\lambda; B) = C_0(B)\hat{S}_{\text{N-}V^0}(\lambda) + C_-(B)\hat{S}_{\text{N-}V^-}(\lambda). \tag{6}$$

$\hat{S}_{\text{N-}V^0}(\lambda)$ and $\hat{S}_{\text{N-}V^-}(\lambda)$ are the normalized base spectra, which are derived from the N-V^0 and N-V^- spectra we obtain earlier in this section by analyzing the spectroscopic results at magnetic fields of 170 and 975 G, such that $\int \hat{S}_{\text{N-}V^0}(\lambda)d\lambda = \int \hat{S}_{\text{N-}V^-}(\lambda)d\lambda = 1$. $C_0(B)$ and $C_-(B)$ quantify the contributions to the PL spectra from N-V^0 and N-V^- states.

By expressing Eq. (6) for magnetic fields B_1 and B_2, and using them in Eqs. (3)–(5), it is straightforward to express f for a change in magnetic field from B_1 to B_2 as

$$f\,(B_1; B_2) = \frac{C_-(B_1)}{C_0(B_1) + C_-(B_1) - C_0(B_2) - C_-(B_2)}. \tag{7}$$

We determine $C_0(B)$ and $C_-(B)$ by fitting the PL spectra measured at different magnetic fields to $A_{\text{N-}V}(\lambda; B)$. The experimental spectrum measured at 170 G and the fit to $A_{\text{N-}V}(\lambda; B)$ are shown in Fig. 3(a). We fit $A_{\text{N-}V}(\lambda; B)$ to spectra measured at different magnetic fields and estimate the values of $C_0(B)$ and $C_-(B)$, which are shown in Fig. 3(b). The plot suggests that N-V^- PL decreases with increasing magnetic field strength, which supports spin-mixing-induced PL reduction, as discussed earlier in this section. At a certain field value, the N-V^- PL reaches a minimum, which indicates the fully-spin-mixed state. However, with a further increase in the magnetic field, we see a slight enhancement in the N-V^- PL, which can happen due to the influence of the magnetic field on the singlet-to-triplet-state transition rate at the excited state of N-V [36]. It is worth noting that there is no observable change in the PL from N-V^0 as a function of magnetic field, which allows us to rewrite Eq. (7) as

$$f\,(B_1; B_2) = \frac{C_-(B_1)}{C_-(B_1) - C_-(B_2)}. \tag{8}$$

To quantify the factor $f\,(B_1; B_2)$ in different magnetic field regimes and intervals, we use the values of $C_-(B_1)$ and $C_-(B_2)$ obtained with Eq. (8) and calculate $f\,(B_1; B_2)$. B_1 is varied from 170 to 550 G, where B_2 is varied from 248 to 975 G. Complete spin mixing, i.e., total depolarization of the electronic spins, depends on the strength, orientation, and relative concentration of N-V with four possible axis orientations in the ensemble. In this case, complete spin mixing happens at 829 G, which corresponds to the minima in the field-dependent $C_-(B)$ values shown in Fig. 3(b) and f values shown in Fig. 3(c). One can see from Fig. 3(c) that $f\,(B_1; B_2)$ decreases with increasing field difference until the fully-spin-mixed state is reached. Afterwards, $f\,(B_1; B_2)$ increases with increasing $(B_2 - B_1)$ due to the N-V excited-state singlet-triplet transition rate dependence on magnetic field [36]. Notably, for the same variation in magnetic field, $f\,(B_1; B_2)$ can take different values, depending on B_1. The data point representing the value of $f\,(170\text{ G}; 975\text{ G}) \approx 6.2$, which we use in our analysis, is denoted by a square box. Equations (4) and (5) suggest that f is small for a large value of $\Delta_{\text{N-}V^-}$. Hence, a lower value of $f\,(B_1; B_2)$ signifies a considerable variation in N-V^- PL upon changing the magnetic field, which suggests that the spectra measured at 170 and 975 G provide a good SNR in our N-V^-–N-V^0 spectral decomposition analysis. By comparing the decomposed N-V^0 and N-V^- spectra we obtain for different values of B_1 and B_2, we conclude that there is no evidence of changes in the shape of the N-V spectra as a function of the strength of the applied field. This supports our assumption that factor f does not depend on λ.

The $f\,(B_1; B_2)$ values that correspond to $B_2 = 829$ G for different B_1 are fitted to the following expression, and the result is shown by the dashed curve in Fig. 3(c):

$$f\,(B_1; B_2) = 3.3 + 195.7e^{-(B_2 - B_1)/150.34}. \tag{9}$$

Equation (9) allows us to estimate the values of $f\,(B_1; B_2)$ for B_1 when $0 < B_1 < 829$ G and for $B_2 = 829$ G.

Our analysis provides the ratio of emissions from N-V^0 and N-V^-, which allows us determining the ratio, $R_{\text{N-}V^-:\text{N-}V^0}$, of the concentrations $C_{\text{N-}V^-}$ and $C_{\text{N-}V^0}$ of the

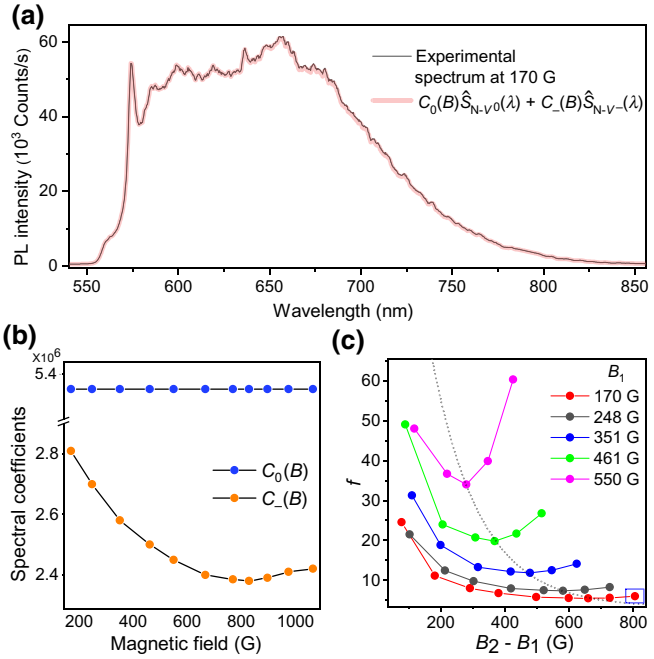

FIG. 3. (a) N-V spectrum (red curve) measured at an applied field of 170 G and its fit to $A_{\text{N-}V}(\lambda; B)$ (black curve). (b) Variation of N-V^- and N-V^0 PL as a function of applied magnetic field strength. (c) Dependence of $f\,(B_1; B_2)$ on magnetic field variation. Dashed curve connects data points that correspond to $B_2 = 829$ G for different B_1 values.

N-V^- and N-V^0 charge states, respectively [32]:

$$R_{\text{N-}V^-:\text{N-}V^0} = \frac{C_{\text{N-}V^-}}{C_{\text{N-}V^0}} = \frac{C_-(B)}{\kappa_\lambda(B) C_0(B)}. \tag{10}$$

The ratio of PL from the N-V^--to-N-V^0 centers is $\kappa_\lambda(B)$, which depends on the applied field strength and excitation wavelength λ. Since in this case $\lambda = 532$ nm, we use $\kappa_{532\text{nm}}(0) = 2.17$ from Ref. [32] in our analysis. Now, using Eq. (8) and the fact that $C_0(B_1) = C_0(B_2)$ we write

$$R_{\text{N-}V^-:\text{N-}V^0} = \frac{C_-(0)}{\kappa_\lambda(0) C_0(0)} = \frac{C_-(B_2)}{\kappa_\lambda(0) C_0(B_2)} \frac{f\,(0; B_2)}{[f\,(0; B_2) - 1]}. \tag{11}$$

The value of $R_{\text{N-}V^-:\text{N-}V^0}$ does not differ for different values of B_2 as the steady-state population of the N-V^- and N-V^0 ensemble do not vary with the strength of the field. For instance, for $B_2 = 829$ G, we calculate $f\,(0; 829\text{ G}) = 4.1$ from Eq. (9). Thus, from Eq. (11), we obtain $R_{\text{N-}V^-:\text{N-}V^0} = 0.271$ at the location where we measure the spectra. Since $R_{\text{N-}V^-:\text{N-}V^0}$ does not change with magnetic field strength [26], Eq. (10) allows us to calculate $\kappa_{532\,\text{nm}}(B) = 1.94$ when $B = 170$ G.

The above protocol of separating out the N-V^- and N-V^0 spectral components can be used to perform charge-state imaging for N-V centers. We assume $I^{\text{low }\mathbf{B}}(X, Y)$ and

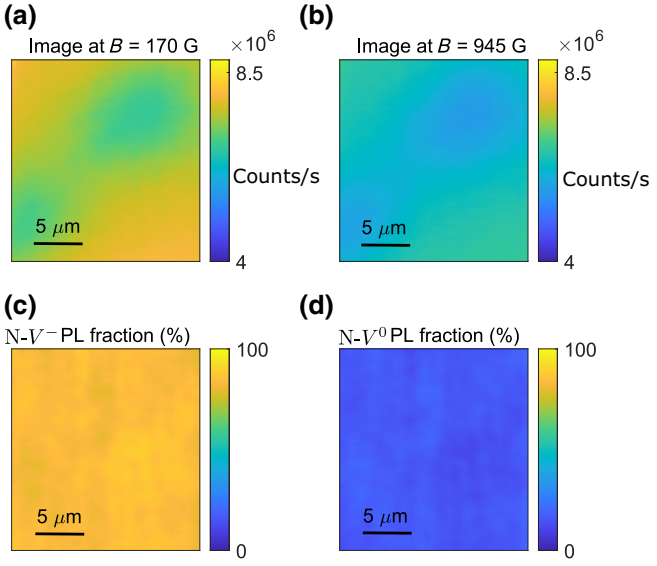

FIG. 4. PL maps for an N-V ensemble at (a) 170 G and (b) 975 G magnetic fields. Contribution of (c) N-V^0 and (d) N-V^- PL to the map shown in (a).

$I^{\text{high }\mathbf{B}}(X, Y)$, as shown in Figs. 4(a) and 4(b), are spatial maps captured for an N-V ensemble in low (170 G) and high (975 G) magnetic fields, and we aim to decompose $I^{\text{low }\mathbf{B}}(X, Y)$ into maps for N-V^- and N-V^0. To enhance the SNR, at each field, the maps are collected 4 times and added up. Provided that, apart from N-V centers, there are no other defect centers or other impurities that generate PL under 532-nm laser excitation, one can write

$$I^{\text{low }\mathbf{B}}(X, Y) = I^{\text{N-}V^0}(X, Y) + I^{\text{N-}V^-}(X, Y), \tag{12}$$

where $I^{\text{N-}V^0}(X, Y)$ and $I^{\text{N-}V^-}(X, Y)$ are the PL matrices that consist of contributions of PL from N-V^0 and N-V^- centers only. Following the arguments made earlier in this section, we can calculate $I^{\text{diff}}(X, Y)$, as

$$I^{\text{diff}}(X, Y) = I^{\text{low }\mathbf{B}}(X, Y) - I^{\text{high }\mathbf{B}}(X, Y), \tag{13}$$

which should be a pure N-V^- PL signal.

For a fixed strength and orientation of the applied field, we measure spectra at arbitrary positions of the diamond sample and observe a nearly uniform ratio of $C_- : C_0$ over the region of microscopy. Hence, assuming that the value $f = 6.2$ does not vary over the 20×20 μm^2 area we measure, we create maps of the charge states N-V^- and N-V^0, $I^{\text{N-}V^-}(X, Y) = f\, I^{\text{diff}}(X, Y)$ and $I^{\text{N-}V^0}(X, Y) = I^{\text{low }\mathbf{B}}(X, Y) - f\, I^{\text{diff}}(X, Y)$, and show their contributions to $I^{\text{low }\mathbf{B}}(X, Y)$ in Figs. 4(c) and 4(d). The maps show that the populations of N-V^- and N-V^0 centers vary spatially in this 20×20 μm^2 area. However, for diamond crystals like the high-pressure high-temperature grown ones, there can be a nonuniform spatial distribution of the N-V^0 :

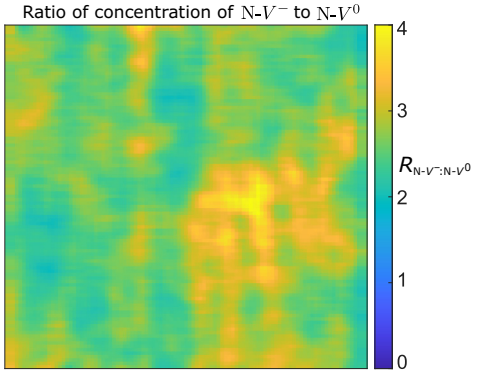

FIG. 5. Mapping ratio of concentrations of N-V^- to N-V^0 centers.

N-V^- population ratio. Hence, one has to take into account spatial variation of factor f in the above mapping analysis. For this purpose, spectral decomposition has to be performed at different positions of the sample, and the spatial variation of factor f has to be determined in the form $f(X,Y)$. We create a map of the ratio of concentrations of N-V^--to-N-V^0 centers at 170 G by using the relation $R_{\text{N-}V^-:\text{N-}V^0}(X,Y) = I^{\text{N-}V^-}(X,Y)/\kappa(B)I^{\text{N-}V^0}(X,Y)$, as shown in Fig. 5. From our earlier analysis, we use $\kappa_{532\text{nm}}(B) = 1.94$ when $B = 170$ G.

IV. OPTICAL-FILTER-BASED SPECTRAL DECOMPOSITION

Here, we demonstrate a protocol to decompose the steady-state N-V^0 and N-V^- signals and construct separate PL images for these two charge states. We capture the PL mapping image of an ensemble of N-V centers extended over an area of $20 \times 20\ \mu\text{m}^2$, which we denote as $M_0(X,Y)$ and show in Fig. 6(a). We capture spectra at different spatial positions of this N-V ensemble and observe the clear signature of the ZPLs for N-V^- and N-V^0. Hence, the $20 \times 20\ \mu\text{m}^2$ PL mapping image consists of signal contributions from both N-V^- and N-V^0, which we like to separate using our method. We express

$$M_0(X,Y) = M_{\text{N-}V^0}(X,Y) + M_{\text{N-}V^-}(X,Y), \tag{14}$$

which signifies that M_0 is the sum of the two component signals $M_{\text{N-}V^0}(X,Y)$ and $M_{\text{N-}V^-}(X,Y)$, which map the signals from N-V^0 and N-V^- centers, respectively. Next, we include a 645-nm long-pass filter (LPF), which has different transmissions for the signals from N-V^0 and N-V^- and record a PL image of the same $20 \times 20\ \mu\text{m}^2$ area. We call this image matrix $M_{\text{LPF}}(X,Y)$ and show it in Fig. 6(b). We write t^0 and t^- for the average transmissivity of the PL signals from N-V^0 and N-V^- through the LPF. We then express $M_{\text{LPF}}(X,Y)$ as

$$M_{\text{LPF}}(X,Y) = t^0 M_{\text{N-}V^0}(X,Y) + t^- M_{\text{N-}V^-}(X,Y). \tag{15}$$

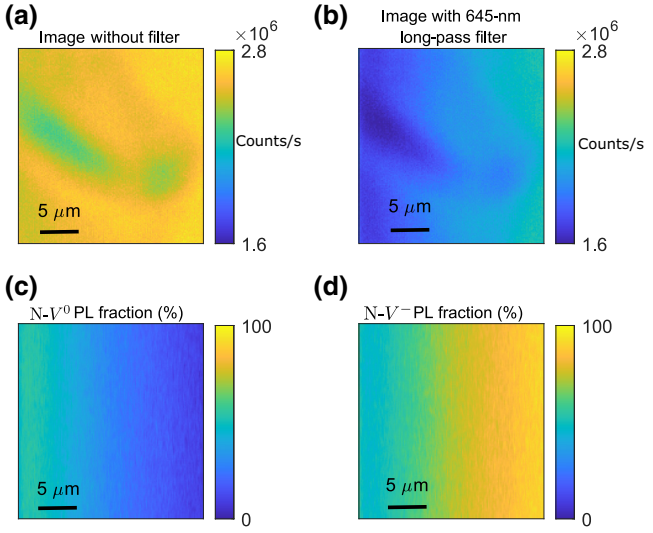

FIG. 6. Measured PL mapping images (a) without and (b) with the 645-nm long-pass filter. Mapping image of the fraction of PL-signal contributions from (c) N-V^0 and (d) N-V^- centers into the image shown in (a), as calculated using our decomposition method.

To calculate t^0 and t^-, we use the decomposed spectra of N-V^0 and N-V^-, shown by the thin red and blue curves in Fig. 7 and the thick red and blue curves, $A^{\text{LPF}}_{\text{N-}V^0}(\lambda)$ and $A^{\text{LPF}}_{\text{N-}V^-}(\lambda)$, in Fig. 7, which represent the spectra after the 645-nm LPF. Thus, the ratio of the integrated area under the filter-modulated curve to the corresponding original spectrum gives us the filter transmitivity:

$$t^0 = \int_{550}^{850} A^{\text{LPF}}_{\text{N-}V^0}(\lambda)d\lambda \Big/ \int_{550}^{850} A_{\text{N-}V^0}(\lambda)d\lambda, \tag{16}$$

$$t^- = \int_{550}^{850} A^{\text{LPF}}_{\text{N-}V^-}(\lambda)d\lambda \Big/ \int_{550}^{850} A^{\text{low}\,\mathbf{B}}_{\text{N-}V^-}(\lambda)d\lambda. \tag{17}$$

Upon solving Eqs. (14) and (15), it is straightforward to calculate $M_{\text{N-}V^0}(X,Y)$ and $M_{\text{N-}V^-}(X,Y)$, which are given by

$$M_{\text{N-}V^0}(X,Y) = \frac{M_{\text{LPF}}(X,Y) - t^- M_0(X,Y)}{t^0 - t^-}, \tag{18}$$

$$M_{\text{N-}V^-}(X,Y) = \frac{t^0 M_0(X,Y) - M_{\text{LPF}}(X,Y)}{t^0 - t^-}. \tag{19}$$

We perform the integration mentioned in Eqs. (16) and (17) in the wavelength range of 550 to 850 nm, which covers $> 99\%$ of the emission spectra (the CCD arrays in the spectrometer cover the wavelength range of 200–1160 nm). The resulting values are $t^0 = 0.3$ and $t^- = 0.8$. Using

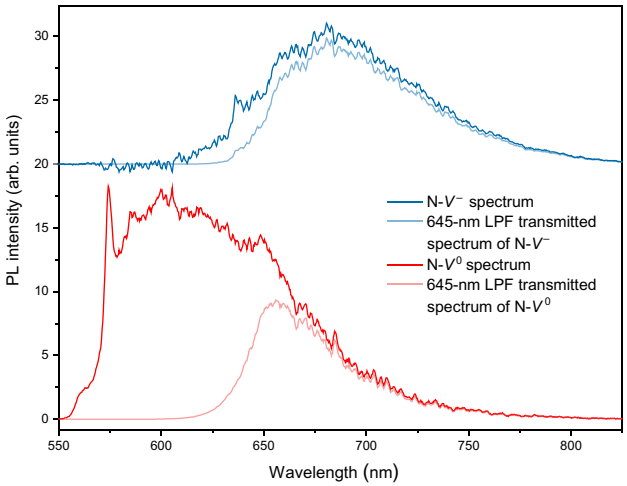

FIG. 7. Extracted N-V^0 spectrum (thin red curve) and its transmission through a 645-nm long-pass filter (thick red curve), extracted N-V^- spectrum (thin blue curve) and its transmission through a 645-nm long-pass filter (thick blue curve).

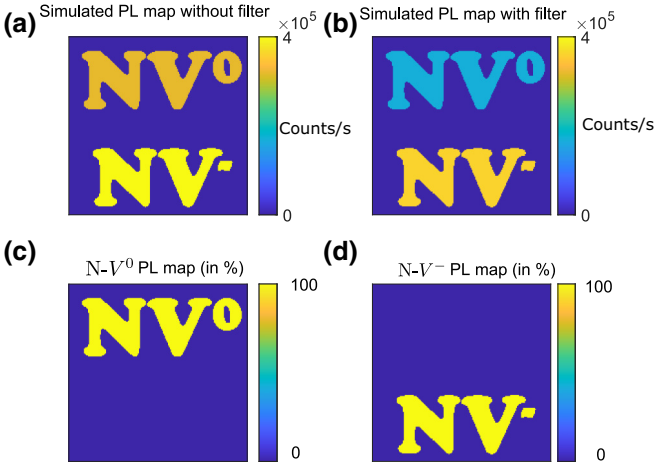

FIG. 8. Simulated PL mapping images (a) without and (b) with the 645-nm long-pass filter. Mapping images for (c) N-V^0 and (d) N-V^- centers decomposed using Eqs. (18) and (19).

these values, we obtain separate maps of $M_{\text{N-}V^0}(X,Y)$ and $M_{\text{N-}V^-}(X,Y)$. Figures 6(c) and 6(d) show the relative contributions of $M_{\text{N-}V^0}(X,Y)$ and $M_{\text{N-}V^-}(X,Y)$ to $M_0(X,Y)$. The images show that, in that part of the sample, there is a linear gradient of N-V^-/N-V^0 concentration.

As an additional check of this method, we decompose a simulated PL matrix that contains signals from both N-V^0 and N-V^-. Figure 8(a) represents the simulated PL mapping image $M_0(X,Y)$, where the pixels inside the letters "NV^0" and "NV$^-$" are assigned to PL signals from N-V^0 ($S_{\text{N-}V^0}$) and N-V^- ($S_{\text{N-}V^-}$), respectively, and rest of the pixels have the value zero. These values of the PL signal represent total count rates. Now we simulate a PL mapping image $M_{\text{LPF}}(X,Y)$, assuming that we place a 645-nm LPF before the detector, while keeping other conditions unchanged. This is expressed by a PL matrix where the pixels are $t^0 S_{\text{N-}V^0}$ and $t^- S_{\text{N-}V^-}$. From Eqs. (18) and (19), using values of t^0 and t^-, we obtain the matrices $M_{\text{N-}V^0}(X,Y)$ and $M_{\text{N-}V^-}(X,Y)$. Figures 8(c) and 8(d) show these maps as fractional contributions to $M_0(X,Y)$. One can observe that Fig. 8(c) comprises N-V^0 PL of equal intensity at the pixel positions at N-V^0 like in $M_0(X,Y)$, whereas Fig. 8(d) contains only N-V^- PL at the pixels corresponding to $M_0(X,Y)$. The pixels with zero value are zero in both $M_{\text{N-}V^0}(X,Y)$ and $M_{\text{N-}V^-}(X,Y)$. Hence, we conclude that our filter-based decomposition protocol can perform charge-state imaging for N-V centers with full efficiency. However, the simulated image, $M_0(X,Y)$, contains fully-spatially-resolved signals from N-V^0 and N-V^-, which allow us to spatially decompose the charge states. For this test, we assume that there are no other sources of PL under 532-nm excitation, apart from N-V centers in one of the two charge states that contribute to the PL. However, in the case of other PL sources, like other color centers, it is possible to modify the method by using additional optical filters. Thus, the method has the flexibility to decompose a PL map composed of spectra of different origins and create PL mapping images for the elementary color centers concerned.

V. DISCUSSION AND OUTLOOK

In case of decomposing spectra over a large area of a diamond sample, our magnetic-field-assisted spectral decomposition method can be advantageous compared with the previously reported microwave-assisted technique [23]. In the microwave-assisted technique, most commonly, a thin copper wire or a resonator fabricated on the diamond substrate is used for microwave (MW) excitation of the N-V. The driving microwave field in diamond is spatially confined for N-V in close ($\sim \mu$m) vicinity of the wire or inside the resonator. This localized excitation introduces a potential MW field inhomogeneity and spatially limits the flexibility of addressing N-V distributed over a large ($\sim$ nm) area [37–39]. Thus, in the case of imaging an N-V ensemble, N-V in different parts of the ensemble can have interactions with the MW field of different strengths due to the MW field inhomogeneity [12,39–41]. To avoid the experimental error caused by nonuniform MW fields, one either has to account for spatial variation in the spectral decomposition and imaging analysis [42] or design MW resonators that can provide uniform MW field strength over the N-V ensemble to be measured [43–46]. However, in our magnetic-field-assisted technique, since the static magnetic field is typically more homogeneous over the sample than the MW field, a uniform distribution of magnetic field over hundreds of μm can easily be obtained using a Helmholtz coil or a permanent bar magnet, which are the most common techniques for applying magnetic

fields. Hence, by moving the microscope objective over the diamond sample using a nanopositioning stage, N-V at different locations of the diamond can be addressed in the homogeneous field. N-V charge-state decomposition over a large diamond substrate can be performed by additionally moving the sample with a micropositioning stage.

Furthermore, the microwave-assisted technique potentially influences N-V charge-state conversion dynamics, which results in a change in steady-state N-V^0 and N-V^- ensemble populations [23]. Hence, to get rid of any N-V^0 (N-V^-) contribution in the extracted N-V^- (N-V^0) spectrum, one needs to perform additional analyses considering a rate-equation model for the composite N-V^0–N-V^- system. However, in our case, the application of a magnetic field does not change the steady-state populations of N-V^0 and N-V^- states; this makes the spectral decomposition analysis straightforward.

Here, we discuss potential applications of our charge-state imaging methods. Since the signal from N-V^0 creates a background PL signal that is insensitive to an external field, an ensemble with significant N-V^0 population reduces the magnetic-field-sensing efficiency [12]. Hence, to tune the charge-state population, one needs to optimize the N-V preparation and processing parameters and determine the spatial distribution of charge states over the diamond. In this context, our charge-state imaging methods can efficiently be employed to perform charge-state mapping of a diamond sample over an area around 1 cm^2. The present paper demonstrates mapping of N-V^0 and N-V^- states over an area of 400 μm^2. A confocal microscope, where the diamond is mounted on a motorized micrometer stage, can image the charge states in different locations of the sample in an automated way using our methods and can combine these images to generate the map for the whole sample with a resolution of < 1 μm. If high-resolution mapping is not necessary, N-V charge states can be mapped in a simplified way by using a wide-field optical setup [47] in place of the confocal microscope. Either filter-based or field-assisted imaging methods can be applied in this context. Thus, for a given N-V ensemble, one can record the change in N-V^- and N-V^0 distributions as a function of the physical conditions and determine the change in charge-state distribution.

In typical magnetic-field-sensing platforms using N-V ensembles, a layer of the sample is prepared over N-V that are a few nanometers below the diamond surface, and the PL signal from N-V is recorded [12]. Knowledge of the spatial distributions of the N-V^0 and N-V^- states over the diamond sample generated by the abovementioned imaging method allows one to choose a suitable N-V ensemble, making sensing more efficient.

Our filter-based imaging method is not specific to N-V but can have more general applications: if a PL image consists of signals from arbitrary emitters, the spectra of which overlap, by choosing a suitable long-, band-, or short-pass optical filter, decomposition of the image for the constituent emitters can be performed using our filter-based method. One needs to input the transmitivities of the signal from the emitters through the chosen optical filter in the analysis.

VI. CONCLUSION

Here, we demonstrate two techniques: a spectral decomposition technique to decompose the spectra of N-V^- and N-V^0, and a deconvolution protocol to create separate PL imaging for N-V^- and N-V^0. Our spectral decomposition technique is based on the response of the PL signal from the N-V^- charge state under the influence of an off-axis magnetic field, whereas the N-V^0 center does not show any observable change in PL as a function of magnetic field. Importantly, for N-V spectra measured for different diamond samples and different magnetic fields, our spectral decomposition method remains applicable. Subsequently, relying on the fact that a 645-nm long-pass filter modulates the N-V^- and N-V^0 signals in different ways, we apply a spectral decomposition protocol and create PL mapping images for N-V^- and N-V^0 centers separately.

On one hand, it is shown that the field-assisted method is able to decompose the N-V^0 and N-V^- spectra efficiently, with hardly any contribution from the N-V^0 (N-V^-) signal in N-V^- (N-V^0) spectra. On the other hand, the filter-based approach is able to decompose the simulated PL map consisting of signals from both N-V^0 and N-V^-. Hence, we conclude that both charge-state mapping methods are efficient in decomposing N-V^0 and N-V^- signals. However, the field-assisted spectral decomposition and imaging technique is specific to N-V centers. The method relies on the energy-level structure of the N-V center and the optical transitions between them as a function of the strength and orientation of an external magnetic field, whereas the filter-based imaging method has the advantage that it can have more general applications in imaging emitters with overlapping PL spectra.

ACKNOWLEDGMENTS

T.S.M. acknowledges funding from DST/SJF/PSA03/2012-13 and DST/ICPS/QuST/2019/Q67. V.S.A. acknowledges support from the European Union Horizon 2020 research and innovation program under Marie Skłodowska-Curie Grant No. 766402.

[1] F. Jelezko and J. Wrachtrup, Single defect centres in diamond: A review, Phys. Status Solidi A **13**, 3207 (2006).
[2] M. W. Doherty, N. B. Manson, P. Delaney, F. Jelezko, J. Wrachtrup, and L. C. L. Hollenberg, The nitrogen-vacancy colour centre in diamond, Phys. Rep. **528**, 1 (2013).

[3] G. Balasubramanian, P. Neumann, D. Twitchen, M. Markham, R. Kolesov, N. Mizuochi, J. Isoya, J. Achard, J. Beck, J. Tissler, *et al.*, Ultralong spin coherence time in isotopically engineered diamond, Nat. Mater. **8**, 383 (2009).

[4] C. Kurtsiefer, S. Mayer, P. Zarda, and H. Weinfurter, Stable Solid-State Source of Single Photons, Phys. Rev. Lett. **85**, 290 (2000).

[5] L. Childress, M. G. Dutt, J. Taylor, A. Zibrov, F. Jelezko, J. Wrachtrup, P. Hemmer, and M. Lukin, Coherent dynamics of coupled electron and nuclear spin qubits in diamond, Science **314**, 281 (2006).

[6] M. V. G. Dutt, L. Childress, L. Jiang, E. Togan, J. Maze, F. Jelezko, A. S. Zibrov, P. R. Hemmer, and M. D. Lukin, Quantum register based on individual electronic and nuclear spin qubits in diamond, Science **316**, 1312 (2007).

[7] T. Chakraborty, J. Zhang, and D. Suter, Polarizing the electronic and nuclear spin of the NV-center in diamond in arbitrary magnetic fields: Analysis of the optical pumping process, New J. Phys. **19**, 073030 (2017).

[8] D. Hopper, H. Shulevitz, and L. Bassett, Spin readout techniques of the nitrogen-vacancy center in diamond, Micromachines **9**, 437 (2018).

[9] A. Sipahigil, R. E. Evans, D. D. Sukachev, M. J. Burek, J. Borregaard, M. K. Bhaskar, C. T. Nguyen, J. L. Pacheco, H. A. Atikian, C. Meuwly, *et al.*, An integrated diamond nanophotonics platform for quantum-optical networks, Science **354**, 847 (2016).

[10] H. Bernien, L. Childress, L. Robledo, M. Markham, D. Twitchen, and R. Hanson, Two-Photon Quantum Interference from Separate Nitrogen Vacancy Centers in Diamond, Phys. Rev. Lett. **108**, 043604 (2012).

[11] P. Neumann, N. Mizuochi, F. Rempp, P. Hemmer, H. Watanabe, S. Yamasaki, V. Jacques, T. Gaebel, F. Jelezko, and J. Wrachtrup, Multipartite entanglement among single spins in diamond, Science **320**, 1326 (2008).

[12] L. Rondin, J.-P. Tetienne, T. Hingant, J.-F. Roch, P. Maletinsky, and V. Jacques, Magnetometry with nitrogen-vacancy defects in diamond, Rep. Prog. Phys. **77**, 056503 (2014).

[13] T. Wolf, P. Neumann, K. Nakamura, H. Sumiya, T. Ohshima, J. Isoya, and J. Wrachtrup, Subpicotesla Diamond Magnetometry, Phys. Rev. X **5**, 041001 (2015).

[14] R. Schirhagl, K. Chang, M. Loretz, and C. L. Degen, Nitrogen-vacancy centers in diamond: Nanoscale sensors for physics and biology, Annu. Rev. Phys. Chem. **65**, 83 (2014).

[15] S. Haziza, N. Mohan, Y. Loe-Mie, A.-M. Lepagnol-Bestel, S. Massou, M.-P. Adam, X. L. Le, J. Viard, C. Plancon, R. Daudin, *et al.*, Fluorescent nanodiamond tracking reveals intraneuronal transport abnormalities induced by brain-disease-related genetic risk factors, Nat. Nanotechnol **12**, 322 (2017).

[16] J. Wang, F. Feng, J. Zhang, J. Chen, Z. Zheng, L. Guo, W. Zhang, X. Song, G. Guo, L. Fan, *et al.*, High-sensitivity temperature sensing using an implanted single nitrogen-vacancy center array in diamond, Phys. Rev. B **91**, 155404 (2015).

[17] P. Neumann, I. Jakobi, F. Dolde, C. Burk, R. Reuter, G. Waldherr, J. Honert, T. Wolf, A. Brunner, J. H. Shim, *et al.*, High-precision nanoscale temperature sensing using single defects in diamond, Nano Lett. **13**, 2738 (2013).

[18] S. Felton, A. Edmonds, M. E. Newton, P. Martineau, D. Fisher, and D. Twitchen, Electron paramagnetic resonance studies of the neutral nitrogen vacancy in diamond, Phys. Rev. B **77**, 081201 (2008).

[19] A. Gali, Theory of the neutral nitrogen-vacancy center in diamond and its application to the realization of a qubit, Phys. Rev. B **79**, 235210 (2009).

[20] F. Casola, T. van der Sar, and A. Yacoby, Probing condensed matter physics with magnetometry based on nitrogen-vacancy centres in diamond, Nat. Rev. Mater. **3**, 1 (2018).

[21] J. F. Barry, J. M. Schloss, E. Bauch, M. J. Turner, C. A. Hart, L. M. Pham, and R. L. Walsworth, Sensitivity optimization for NV-diamond magnetometry, Rev. Mod. Phys. **92**, 015004 (2020).

[22] K. Yahata, Y. Matsuzaki, S. Saito, H. Watanabe, and J. Ishi-Hayase, Demonstration of vector magnetic field sensing by simultaneous control of nitrogen-vacancy centers in diamond using multi-frequency microwave pulses, Appl. Phys. Lett. **114**, 022404 (2019).

[23] D. A. Craik, P. Kehayias, A. Greenspon, X. Zhang, M. Turner, J. Schloss, E. Bauch, C. Hart, E. Hu, and R. Walsworth, Microwave-Assisted Spectroscopy Technique for Studying Charge State in Nitrogen-Vacancy Ensembles in Diamond, Phys. Rev. Appl. **14**, 014009 (2020).

[24] N. Aslam, G. Waldherr, P. Neumann, F. Jelezko, and J. Wrachtrup, Photo-induced ionization dynamics of the nitrogen vacancy defect in diamond investigated by single-shot charge state detection, New J. Phys. **15**, 013064 (2013).

[25] R. Giri, F. Gorrini, C. Dorigoni, C. Avalos, M. Cazzanelli, S. Tambalo, and A. Bifone, Coupled charge and spin dynamics in high-density ensembles of nitrogen-vacancy centers in diamond, Phys. Rev. B **98**, 045401 (2018).

[26] R. Giri, C. Dorigoni, S. Tambalo, F. Gorrini, and A. Bifone, Selective measurement of charge dynamics in an ensemble of nitrogen-vacancy centers in nanodiamond and bulk diamond, Phys. Rev. B **99**, 155426 (2019).

[27] S. Dhomkar, J. Henshaw, H. Jayakumar, and C. A. Meriles, Long-term data storage in diamond, Sci. Adv. **2**, e1600911 (2016).

[28] K. R. K. Rao, Y. Wang, J. Zhang, and D. Suter, Optimal photon energies for initialization of hybrid spin quantum registers of nitrogen-vacancy centers in diamond, Phys. Rev. A **101**, 013835 (2020).

[29] N. B. Manson, M. Hedges, M. S. Barson, R. Ahlefeldt, M. W. Doherty, H. Abe, T. Ohshima, and M. J. Sellars, NV^{-}–N^{+} pair centre in 1b diamond, New J. Phys. **20**, 113037 (2018).

[30] T. L. McCormick, W. Jackson, and R. Nemanich, The characterization of strain, impurity content, and crush strength of synthetic diamond crystals, J. Mater. Res. **12**, 253 (1997).

[31] X.-D. Chen, C.-H. Dong, F.-W. Sun, C.-L. Zou, J.-M. Cui, Z.-F. Han, and G.-C. Guo, Temperature dependent energy level shifts of nitrogen-vacancy centers in diamond, Appl. Phys. Lett. **99**, 161903 (2011).

[32] S. T. Alsid, J. F. Barry, L. M. Pham, J. M. Schloss, M. F. O'Keeffe, P. Cappellaro, and D. A. Braje, Photoluminescence Decomposition Analysis: A Technique to Characterize N-V Creation in Diamond, Phys. Rev. Appl. **12**, 044003 (2019).

[33] N. D. Lai, D. Zheng, F. Jelezko, F. Treussart, and J.-F. Roch, Influence of a static magnetic field on the photoluminescence of an ensemble of nitrogen-vacancy color centers in a diamond single-crystal, Appl. Phys. Lett. **95**, 133101 (2009).

[34] J. Tetienne, L. Rondin, P. Spinicelli, M. Chipaux, T. Debuisschert, J. Roch, and V. Jacques, Magnetic-field-dependent photodynamics of single NV defects in diamond: An application to qualitative all-optical magnetic imaging, New J. Phys. **14**, 103033 (2012).

[35] R. Epstein, F. Mendoza, Y. Kato, and D. Awschalom, Anisotropic interactions of a single spin and dark-spin spectroscopy in diamond, Nat. Phys. **1**, 94 (2005).

[36] M. Capelli, P. Reineck, D. Lau, A. Orth, J. Jeske, M. Doherty, T. Ohshima, A. Greentree, and B. Gibson, Magnetic field-induced enhancement of the nitrogen-vacancy fluorescence quantum yield, Nanoscale **9**, 9299 (2017).

[37] E. V. Levine, M. J. Turner, P. Kehayias, C. A. Hart, N. Langellier, R. Trubko, D. R. Glenn, R. R. Fu, and R. L. Walsworth, Principles and techniques of the quantum diamond microscope, Nanophotonics **8**, 1945 (2019).

[38] M. J. Turner, N. Langellier, R. Bainbridge, D. Walters, S. Meesala, T. M. Babinec, P. Kehayias, A. Yacoby, E. Hu, M. Lončar, *et al.*, Magnetic Field Fingerprinting of Integrated-Circuit Activity with a Quantum Diamond Microscope, Phys. Rev. Appl. **14**, 014097 (2020).

[39] K. Mizuno, H. Ishiwata, Y. Masuyama, T. Iwasaki, and M. Hatano, Simultaneous wide-field imaging of phase and magnitude of AC magnetic signal using diamond quantum magnetometry, Sci. Rep. **10**, 1 (2020).

[40] G. Mariani, S. Nomoto, S. Kashiwaya, and S. Nomura, System for the remote control and imaging of MW fields for spin manipulation in NV centers in diamond, Sci. Rep. **10**, 1 (2020).

[41] L. M. Pham, D. Le Sage, P. L. Stanwix, T. K. Yeung, D. Glenn, A. Trifonov, P. Cappellaro, P. R. Hemmer, M. D. Lukin, H. Park, *et al.*, Magnetic field imaging with nitrogen-vacancy ensembles, New J. Phys. **13**, 045021 (2011).

[42] Y. Vaknin, B. Tratzmiller, T. Gefen, I. Schwartz, M. Plenio, and A. Retzker, Robustness of the NV-NMR Spectrometer Setup to Magnetic Field Inhomogeneities, Phys. Rev. Lett. **125**, 110502 (2020).

[43] K. Bayat, J. Choy, M. Farrokh Baroughi, S. Meesala, and M. Loncar, Efficient, uniform, and large area microwave magnetic coupling to NV centers in diamond using double split-ring resonators, Nano Lett. **14**, 1208 (2014).

[44] O. R. Opaluch, N. Oshnik, R. Nelz, and E. Neu, Optimized planar microwave antenna for nitrogen vacancy center based sensing applications, Nanomaterials **11**, 2108 (2021).

[45] N. Zhang, C. Zhang, L. Xu, M. Ding, W. Quan, Z. Tang, and H. Yuan, Microwave magnetic field coupling with nitrogen-vacancy center ensembles in diamond with high homogeneity, Appl. Magn. Reson. **47**, 589 (2016).

[46] V. Yaroshenko, A. Zalogina, D. Zuev, P. Kapitanova, and I. Shadrivov, in *J. Phys. Conf. Ser.* (IOP Publishing, Bristol, United Kingdom, 2018), Vol. 1092, p. 012168.

[47] V. K. Sewani, H. H. Vallabhapurapu, Y. Yang, H. R. Firgau, C. Adambukulam, B. C. Johnson, J. J. Pla, and A. Laucht, Coherent control of NV^- centers in diamond in a quantum teaching lab, Am. J. Phys. **88**, 1156 (2020).